Progress In Electromagnetics Research, Vol. 142, 75–105, 2013

ATTENUATION CONSTANTS OF RADIO WAVES IN LOSSY-WALLED RECTANGULAR WAVEGUIDES

Chenming Zhou*, Joseph Waynert, Timothy Plass, and Ronald Jacksha

National Institute for Occupational Safety and Health, Pittsburgh, PA 15236, USA

Abstract—At the ultra-high frequencies (UHF) common to portable radios, the mine tunnel acts as a dielectric waveguide, directing and absorbing energy as a radio signal propagates. Understanding radio propagation behavior in a dielectric waveguide is critical for designing reliable, optimized communication systems in an underground mine. One of the major parameters used to predict the power attenuation in lossy waveguides is the attenuation constant. In this paper, we theoretically and experimentally investigate the attenuation constants for a rectangular waveguide with dielectric walls. We provide a new derivation of the attenuation constant based on the classic Fresnel reflection coefficients. The new derivation takes advantage of ray representation of plane waves and provides more insight into understanding radio attenuation in tunnels. We also investigate the impact of different parameters on the attenuation constant, including the tunnel transverse dimensions, permittivity, conductivity, frequency, and polarization, with an aim to find their theoretical optimal values that result in the minimum power loss. Additionally, measurements of the attenuation constants of the dominant mode at different frequencies (455, 915, 2450, and 5800 MHz) for a straight concrete tunnel are presented and compared to theoretical predictions. It is shown that the analytical results match the measured results very well at all four frequencies.

Received 17 June 2013, Accepted 6 August 2013, Scheduled 20 August 2013

* Corresponding author: Chenming Zhou (czhou@cdc.gov).

1. INTRODUCTION

Radio propagation in tunnel-like environments, such as street canyons [1], indoor hallways [2, 3], road/subway tunnels [4–6], and underground coal mines [7, 8] has been widely investigated. Interest in tunnel communications can be traced back to the 1940s [9], with a dramatic spike in the 1970s [10, 11] driven by the need for communication among workers in underground mine tunnels. This interest was recently reinforced by the passage of the Mine Improvement and New Emergency Response Act (MINER Act) [12], legislation enacted by the U.S. Congress as a reaction to a series of mine tragedies occurring in 2006. The MINER Act requires that wireless communication systems be installed in all U.S. underground coal mines. The performance of these wireless systems is highly dependent on the radio propagation behavior in the confined environment of tunnels. Extensive measurements were taken by researchers at the National Institute for Occupational Safety and Health (NIOSH) to investigate the RF propagation mechanism [13, 14] in tunnels.

A tunnel is often modeled as a hollow waveguide surrounded by dielectric media. Rectangular and circular tunnels are perhaps the two most common tunnel types and have been well-investigated. It is shown in [15] that circular waveguides allow for a rigorous derivation of the analytical expression of the propagating modes. Determining the exact analytical solution of a rectangular waveguide, however, is not possible due to the difficulty in matching boundary conditions. Instead, approximate solutions were investigated with an analytical result obtained in [16] where boundary conditions were only matched along the four sides of the hollow regions. For the derivation in both [15] and [16], the wavelengths of interest were assumed to be small compared to the tunnel dimensions. In many practical tunnels, the ceiling is often arch-shaped while the floor is flat. Since this hybrid shape cannot be easily described by a canonical coordinate system, no analytical formulation of the field distribution is available. As a result, an arched tunnel is often approximated by either a circular tunnel [17] or a rectangular tunnel [13]. Efforts have been made to tackle the arched tunnel directly without an approximation, for example by a ray-density normalization technique proposed in [18], but the computation complexity is relatively high and its accuracy remains to be validated by more measurements.

Compared to a waveguide with perfect electric conductor (PEC) walls which reflect all waves back to the waveguide, it is found that modes in waveguides with dielectric walls are all "lossy modes"; any wave that impinges on a tunnel wall is partially transmitted

into the surrounding dielectric media and partially reflected back to the tunnel. The energy loss of each mode in the waveguide is characterized by the attenuation constant associated with that mode. The analytical expression for the attenuation constant of a hollow dielectric rectangular tunnel was first derived in [10]. The same result was also later obtained in [16] and [19], although in a slightly different expression. So far, all the derivations of the attenuation constant have been based on wave theories involved in directly solving Maxwell equations.

In this paper, we revisit the attenuation constant of a dielectric rectangular tunnel and show that it can be derived based on the well-known Fresnel reflection coefficients. The new derivation based on Fresnel reflection coefficients is more intuitive and provides more insight as compared to published results which were based on directly solving Maxwell equations. The derivation presented in this paper clearly shows that the path loss associated with tunnel propagation is solely caused by the energy loss when rays are reflected from the four dielectric walls of the tunnel. As a result, the propagation loss is highly dependent on the reflection coefficient when rays are reflected from dielectric walls. The reflection coefficient is known to be dependent on the electrical properties of the walls, polarization and frequency, and tunnel dimensions. We analyze the impact of these parameters on the attenuation constant. Our analysis differs from other published work (e.g., [20]) in the sense that we aim to find the theoretical optimal value of each parameter for minimum power losses, and thus gain insight into the factors controlling RF signal path loss.

In addition to the analytical form derived, the attenuation constant of the dominant mode can also be evaluated based on simulated or measured power distributions along the tunnel, provided that the separation distance is sufficiently long such that all the higher modes are significantly attenuated as compared to the dominant mode which has the lowest attenuation constant [13]. For a sufficiently long distance, the power decays linearly with the distance and the slope of the decay is the attenuation constant of the dominant mode. In this paper, we compare the attenuation constant computed based on three different methods: the modal method, ray tracing method, and measurement. We show that all three methods compare well with each other.

Geometrical ray tracing method is employed to obtain the simulated power distributions in tunnels. The ray tracing method was originally proposed by Mahmoud and Wait in 1974 for modeling electromagnetic wave propagation in rectangular mine tunnels [11]. Since then the method has been widely used by researchers for different

purposes. For example, it was used for predicting delay spread in [21] and evaluating tunnel field distribution in [22]. Recently, Sun and Akyildiz adopted it for modeling the propagation in underground mines and road tunnels [23]. In this paper, we will use the ray tracing method to obtain the simulated power distribution in the target rectangular tunnel, from which the average attenuation constant can be estimated.

Measurements were taken to determine the propagation attenuation constant in a straight concrete tunnel. Power distributions along the center of the tunnel were measured at four different frequencies (455, 915, 2450, and 5800 MHz) that are widely used in current commercial communication systems. At each frequency, both the horizontal and vertical polarization cases were measured.

2. ATTENUATION CONSTANT FOR AN EMPTY DIELECTRIC RECTANGULAR WAVEGUIDE

Consider a straight hollow waveguide with rectangular cross-sectional dimensions ($2b$ and $2a$ as depicted in Fig. 1).

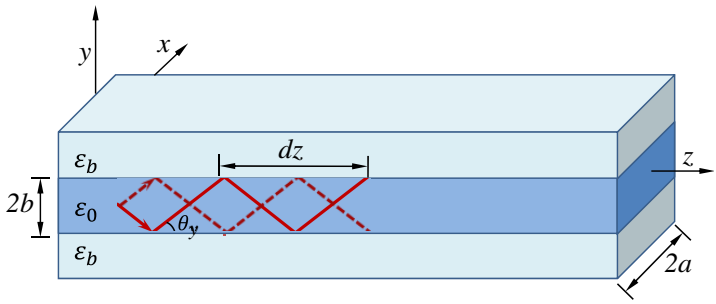

Figure 1. Geometry of the rectangular dielectric waveguide.

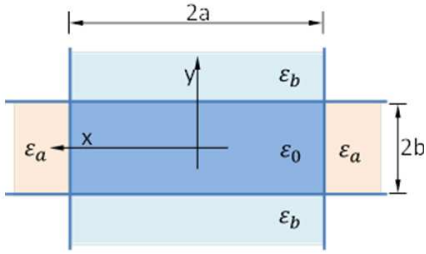

Figure 2. Cross section of the waveguide with four dielectric walls.

Let ε_0 denote the permittivity of air, and $\varepsilon_{a,b}$ the complex permittivity of the vertical and horizontal walls surrounding the waveguide, respectively. The coordinate system is oriented in the center of the waveguide cross section, with x horizontal, y vertical, and z down the waveguide. The cross section of the waveguide is illustrated in Fig. 2. The permeability of all media is assumed to be the same and equal to that of the free space μ_0.

2.1. Electric Field Polarized Predominantly in the Horizontal Direction (x Direction)

For a horizontally polarized signal source, the main component of the E field at an arbitrary observation point $R(x, y, z)$ within the tunnel can be expressed as [16]

$$\begin{aligned} E_x \;=\; & \left\{ \sin\left(k_x x + \varphi_x\right) + \sin\left[\frac{j\bar{\varepsilon}_a}{ka\sqrt{\bar{\varepsilon}_a - 1}} k_x x\right] \cos\left(k_x x + \varphi_x\right) \right\} \\ & \times \left\{ \cos(k_y y + \varphi_y) - \sin\left[\frac{j}{kb\sqrt{\bar{\varepsilon}_b - 1}} k_y y\right] \sin(k_y y + \varphi_y) \right\} e^{-j\tilde{k}_z z} \quad (1) \end{aligned}$$

where $k_x = \frac{m\pi}{2a}$, $k_y = \frac{n\pi}{2b}$, and $\tilde{k}_z = \beta_{m,n} - j\alpha_{m,n}$ are the wave vector components along the x, y, and z axis, respectively. Here, $\beta_{m,n}$ is the phase constant and $\alpha_{m,n}$ is the attenuation constant which characterizes the signal attenuation along the tunnel axial distance (z axis). Note that $\alpha_{m,n}$ is sometimes also referred to as the modal attenuation factor (MAF) [17, 24]. Additionally, $\bar{\varepsilon}_{a,b}$ are relative dielectric constants defined by $\bar{\varepsilon}_{a,b} = \varepsilon_{a,b}/\varepsilon_0$, and $k = 2\pi/\lambda$ is the wave number in free space, with λ denoting the wavelength. It should be noted that the time-dependence factor $e^{-j\omega t}$ has been dropped in (1) for simplicity. The two axillary angles $\varphi_{x,y}$ are defined by

$$\begin{aligned} \varphi_x &= \begin{cases} 0 & m \text{ is even} \\ \pi/2 & m \text{ is odd} \end{cases} \\ \varphi_y &= \begin{cases} 0 & n \text{ is odd} \\ \pi/2 & n \text{ is even} \end{cases} \end{aligned} \quad (2)$$

For electrical small tunnels where $ka \gg 1$ and $kb \gg 1$, (1) can be reduced to

$$E_x \approx \sin\left(\tilde{k}_x x + \varphi_x\right) \cos\left(\tilde{k}_y y + \varphi_y\right) e^{-j\tilde{k}_z z} \quad (3)$$

where the complex wave vector components $\tilde{k}_{x,y}$ are defined as

$$\begin{aligned} \tilde{k}_x &= k_x + \frac{j\bar{\varepsilon}_a}{ka\sqrt{\bar{\varepsilon}_a - 1}} k_x \\ \tilde{k}_y &= k_y + \frac{j}{kb\sqrt{\bar{\varepsilon}_b - 1}} k_y \end{aligned} \quad (4)$$

It is found that the wave vector components $\tilde{k}_{x,y}$ for a dielectric waveguide are the same as the wave vector components $k_{x,y}$ for a metal waveguide, except for a small imaginary part. It is this imaginary part that contributes to the power loss in a dielectric waveguide. It is also observed that the expressions of the imaginary part, $\bar{\varepsilon}_a/\sqrt{\bar{\varepsilon}_a - 1}$ and $1/\sqrt{\bar{\varepsilon}_b - 1}$, are similar to the forms of the Fresnel reflection coefficients corresponding to the horizontal and vertical polarizations, with the electrical field being normal to one boundary and parallel to the other. It is this observation that motivates us to re-derive the attenuation constant based on Fresnel reflection coefficients.

We ignore the small imaginary part in $\tilde{k}_{x,y}$ for now and later we will introduce a reflection coefficient to compensate for the power loss of the rays as they are reflected from a dielectric wall. As a result, (3) can be simplified as

$$E_x \approx \sin(k_x x + \varphi_x)\cos(k_y y + \varphi_y)e^{-jk_z z} \tag{5}$$

For the dominant $EH_{1,1}$ mode, E_x can be expressed as

$$E_x = \cos(k_x x)\cos(k_y y)e^{-jk_z z} \tag{6}$$

Note that (6) is consistent with Eq. (1) in [10], except that a constant E_0 is included in [10] to characterize the transmitted power. Unless stated else, the electric field in this paper represents a normalized field relative to the transmitted field. Additionally, the location of the transmitter is characterized by a coupling factor in [25] where the insertion loss of a half-wave dipole antenna is considered. A more general form of Eq. (5) including both the locations of the transmitter and receiver can be found in [23, 26, 27].

It is worth noting that, unlike a metal waveguide, a rectangular waveguide with dielectric walls supports neither TM nor TE modes. In other words, a longitudinal component E_z, in additional to the transverse components, is always required in order to satisfy the boundary conditions. The longitudinal component E_z, however, is usually small compared to E_x. E_z can be expressed as [16]

$$E_z = -j\left(\frac{m\lambda}{4a}\right)\cos\left(k_x x + \varphi_x\right)\cos\left(k_y y + \varphi_y\right)e^{-jk_z z} \tag{7}$$

As a special case when $m = 1$ and $n = 1$, E_z of the dominant $EH_{1,1}$ mode can be calculated as

$$\begin{aligned} E_z &= j\left(\frac{\lambda}{4a}\right)\sin(k_x x)\cos(k_y y)e^{-jk_z z} \\ &\approx j\left(\frac{k_x}{k_z}\right)\sin(k_x x)\cos(k_y y)e^{-jk_z z} \end{aligned} \tag{8}$$

Note that (8) is consistent with Eq. (A3) in [10].

Recall that cosine and sine functions can be expressed as weighted sums of the exponential function according to Euler-formula,

$$\begin{aligned} \cos k_x x &= \frac{e^{jk_x x} + e^{-jk_x x}}{2} \\ \sin k_x x &= \frac{e^{jk_x x} - e^{-jk_x x}}{2j} \end{aligned} \tag{9}$$

Applying the identity of (9) into (5) leads to

$$\begin{aligned} E_x \;=\; & \frac{j}{4} e^{-j|\varphi_x - \varphi_y|} \\ & \left[\begin{array}{l} e^{j(k_x x + k_y y - k_z z)} + (-1)^{n+1} e^{j(k_x x - k_y y - k_z z)} \\ + (-1)^{m+1} e^{j(-k_x x + k_y y - k_z z)} + (-1)^{m-n} e^{j(-k_x x - k_y y - k_z z)} \end{array} \right] \end{aligned} \tag{10}$$

Note that E_x in (10) can be viewed as a mix of the four plane waves (rays) with each described by an exponential function. Two examples of the rays, $e^{-j(k_z z - k_x x - k_y y)}$ and $e^{-j(k_z z - k_x x + k_y y)}$, are illustrated in Fig. 1 as red dashed and solid lines, respectively. Each ray impinges on the roof and floor of the tunnel with the same angle:

$$\theta_y = \arcsin(k_y/k) \tag{11}$$

The four rays also undergo reflections from the two side walls with an incident angle of

$$\theta_x = \arcsin(k_x/k) \tag{12}$$

Since both k_x and k_y are small compared to k, we can approximate θ_y as

$$\theta_y \approx \frac{k_y}{k} = \frac{n\lambda}{4b} \tag{13}$$

Similarly, the incidence angle of the four rays on the two side walls can be approximated as

$$\theta_x \approx \frac{m\lambda}{4a} \tag{14}$$

Note that the same assumption of grazing incidence has been made in both (13) and (14). The grazing incidence assumption is valid if the wavelength of interest is small compared to the tunnel transverse dimensions.

Between two successive reflections on the roof/floor, the ray travels an axial distance of dz which can be calculated as

$$dz = \frac{4b\cos(\theta_x)}{\tan(\theta_y)} \approx \frac{16b^2}{n\lambda} \tag{15}$$

The number of reflections on roof/floor that the four rays undergo before they reach the receivers can be computed by

$$N_y = \frac{z}{dz} \approx \frac{n\lambda z}{16b^2} \tag{16}$$

Similarly, the number of reflections on the two side walls is

$$N_x \approx \frac{m\lambda z}{16a^2} \tag{17}$$

Note that within the distance z, the ray undergoes N_y reflections on both the side walls and thus $2N_y$ reflections totally in the vertical dimension. Similarly, the number of reflections in the horizontal dimension is $2N_x$. The attenuation of the E field caused by all the reflections can be expressed as

$$E_L = \left| \rho_{//}^{2N_x} \cdot \rho_{\perp}^{2N_y} \right| \tag{18}$$

where $|\cdot|$ denotes the magnitude of the argument, and the two reflection coefficients corresponding to the perpendicular and parallel polarizations under the grazing incidence can be expressed as [11]

$$\rho_{\perp,//} = \frac{\cos\theta_{\perp,//} - \Delta_{\perp,//}}{\cos\theta_{\perp,//} + \Delta_{\perp,//}} \tag{19}$$

where

$$\begin{aligned} \Delta_{//} &= \frac{\sqrt{\bar{\varepsilon}_a - \sin^2\theta_{//}}}{\bar{\varepsilon}_a} \\ \Delta_{\perp} &= \sqrt{\bar{\varepsilon}_b - \sin^2\theta_{\perp}} \end{aligned} \tag{20}$$

Here, $\Delta_{\perp,//}$ is a quantity related with the effective surface impedance, and $\theta_{\perp,//}$ is the incidence angle corresponding to electric field being in the plane of incidence (parallel) and normal to the plane of incidence (perpendicular) polarizations, respectively. The angle $\theta_{\perp,//}$ can be expressed as:

$$\theta_{\perp,//} = \frac{\pi}{2} - \theta_{y,x} \tag{21}$$

Note that the reflection coefficients under the grazing incidence condition in (19) are in a slightly different form than the general Fresnel reflection coefficients given in text books such as [28]. Comparing (19) with the reflection coefficients in [28] shows that the two are identical for the horizontal polarization case but have a 180-degree phase difference for the vertical polarization case. This difference is due to the different definitions of the positive direction for the reflected

waves. For a vertically polarized wave, the definition of the positive electric field of the reflected wave is reversed compared with that of the incident wave (under grazing incidences). Therefore, a negative sign is manually introduced in the equation to compensate for the inversion of the positive direction.

For grazing incidence ($\cos\theta_{\perp,//} \ll \Delta_{\perp,//}$), we can make the following approximations:

$$\begin{aligned}
\rho_{\perp,//} &= -\left(1 - \frac{2\cos\theta_{\perp,//}}{\cos\theta_{\perp,//} + \Delta_{\perp,//}}\right) \\
&\approx -\exp\left(\frac{-2\cos\theta_{\perp,//}}{\cos\theta_{\perp,//} + \Delta_{\perp,//}}\right) \\
&\approx -\exp\left(\frac{-2\cos\theta_{\perp,//}}{\Delta_{\perp,//}}\right) \qquad (22)
\end{aligned}$$

$$\Delta_{//} \approx \frac{\sqrt{\bar{\varepsilon}_a - 1}}{\bar{\varepsilon}_a} \qquad (23)$$

$$\Delta_{\perp} \approx \sqrt{\bar{\varepsilon}_b - 1} \qquad (24)$$

Substituting (16), (17), (19), (23), and (24) into (18) leads to

$$\begin{aligned}
E_L &\approx \left|\exp\left\{-4\left(\frac{\sin\theta_x N_x}{\Delta_{//}} + \frac{\sin\theta_y N_y}{\Delta_{\perp}}\right)\right\}\right| \\
&\approx \left|\exp\left\{-\left[\frac{1}{a}\left(\frac{m\lambda}{4a}\right)^2 \frac{1}{\Delta_{//}} + \frac{1}{b}\left(\frac{n\lambda}{4b}\right)^2 \frac{1}{\Delta_{\perp}}\right] z\right\}\right| \\
&= \exp\left\{-\left[\frac{1}{a}\left(\frac{m\lambda}{4a}\right)^2 \mathrm{Re}\left\{\frac{1}{\Delta_{//}}\right\} + \frac{1}{b}\left(\frac{n\lambda}{4b}\right)^2 \mathrm{Re}\left\{\frac{1}{\Delta_{\perp}}\right\}\right] z\right\} \\
&= \exp\left\{-\frac{z}{a}\left(\frac{m\lambda}{4a}\right)^2 \mathrm{Re}\left\{\frac{\bar{\varepsilon}_a}{\sqrt{\bar{\varepsilon}_a - 1}}\right\} - \frac{z}{b}\left(\frac{n\lambda}{4b}\right)^2 \mathrm{Re}\left\{\frac{1}{\sqrt{\bar{\varepsilon}_b - 1}}\right\}\right\} \\
&= \exp\left\{-\alpha^H_{m,n} z\right\} \qquad (25)
\end{aligned}$$

where the attenuation constant $\alpha^H_{m,n}$ is written as

$$\alpha^H_{m,n} = \frac{1}{a}\left(\frac{m\lambda}{4a}\right)^2 \mathrm{Re}\left\{\frac{\bar{\varepsilon}_a}{\sqrt{\bar{\varepsilon}_a - 1}}\right\} + \frac{1}{b}\left(\frac{n\lambda}{4b}\right)^2 \mathrm{Re}\left\{\frac{1}{\sqrt{\bar{\varepsilon}_b - 1}}\right\} \qquad (26)$$

Note that (26) is exactly the same as the attenuation constant derived in [16].

So far we have only derived the attenuation constant for the x component of the electrical field. To obtain the power attenuation

rate, the attenuation constant of the composite electrical field, $E = \sqrt{E_x^2 + E_y^2 + E_z^2}$, must be calculated. Based on (6) and (7), it is straightforward that E_z and E_x share the same exponent. To satisfy the Maxwell equations, the electrical field along the Y axis (E_y) is zero. Therefore, the attenuation constant of the composite electrical field can be characterized by the same attenuation constant $\alpha_{m,n}$ as that of the E_x. For the dominant $EH_{1,1}$ mode, the power attenuation constant $\hat{\alpha}_{1,1}$ in dB/m can be written as

$$\begin{aligned}\hat{\alpha}_{m,n}^{H} &= -\frac{20\log_{10}(E_L)}{z} \\ &= 20\log_{10} e^{\alpha_{m,n}^{H}} \\ &= 4.343\lambda^2\left[\frac{m^2}{(2a)^3}\mathrm{Re}\left\{\frac{\bar{\varepsilon}_a}{\sqrt{\bar{\varepsilon}_a - 1}}\right\} + \frac{n^2}{(2b)^3}\mathrm{Re}\left\{\frac{1}{\sqrt{\bar{\varepsilon}_b - 1}}\right\}\right] \quad (27)\end{aligned}$$

Eq. (27) is identical with the power attenuation constant derived in [10].

2.2. Electric Field Polarized Predominantly in the Vertical Direction (y Direction)

For a vertically polarized mode $EH_{m,n}$, the attenuation constant of the electrical field can be readily obtained by exchanging a and b, along with m and n in the right side of (26):

$$\alpha_{m,n}^{V} = \frac{1}{b}\left(\frac{n\lambda}{4b}\right)^2 \mathrm{Re}\left\{\frac{\bar{\varepsilon}_b}{\sqrt{\bar{\varepsilon}_b - 1}}\right\} + \frac{1}{a}\left(\frac{m\lambda}{4a}\right)^2 \mathrm{Re}\left\{\frac{1}{\sqrt{\bar{\varepsilon}_a - 1}}\right\} \quad (28)$$

Similarly, the power attenuation constant in dB/m for the vertical polarized signals can be expressed as:

$$\hat{\alpha}_{m,n}^{V} = 4.343\lambda^2\left[\frac{n^2}{(2b)^3}\mathrm{Re}\left\{\frac{\bar{\varepsilon}_b}{\sqrt{\bar{\varepsilon}_b - 1}}\right\} + \frac{m^2}{(2a)^3}\mathrm{Re}\left\{\frac{1}{\sqrt{\bar{\varepsilon}_a - 1}}\right\}\right] \quad (29)$$

3. DETERMINATION THE ATTENUATION CONSTANT BASED ON GEOMETRICAL RAY TRACING

In addition to the analytical forms shown in (26) and (28) which are usually referred to as the modal method, the geometrical ray tracing method is often used to model the propagation in straight tunnels. Based on geometrical ray tracing, the field at any point within a tunnel can be obtained as a summation of the rays coming from all possible paths from the transmitter to the receiver. Therefore, finding those ray paths is critical for the ray tracing method. Two

algorithms, the brute force ray tracing (sometime also referred to as the Shooting and Bouncing Ray (SBR) algorithm) and the image theory based algorithm, are generally used for this purpose. The SBR algorithm [29, 30] is suitable for ray tracing in complex environments, but the computation complexity is relatively high and the traced results could be sensitive to some of the parameters chosen in the simulation. The image-based ray tracing is a clever alternative for environments with highly symmetrical geometries and will be used to model the tunnel propagation in this paper.

3.1. Image Theory

According to image theory, all the reflected rays can be viewed as rays directly launched from different images of the source, with their field amplitudes modified by the proper reflection coefficients. Those two-dimensional images are located within the same x-y plane as the source, with their coordinates given by [13]:

$$\begin{aligned} x_u &= 2ua + (-1)^u x_0 \\ y_v &= 2vb + (-1)^v y_0 \end{aligned} \tag{30}$$

where the integers u and v represent the number of reflections that the ray undergoes relative to the vertical and horizontal walls, respectively. The sign of u and v indicate whether the image is located on the positive or negative side of the x and y axis, respectively. Note that as a special case when $u = v = 0$, the image becomes the source itself which is assumed to be located at $S(x_0, y_0, 0)$.

3.2. Ray Tracing Based Electrical Field Representation

3.2.1. Horizontal Polarization

For a horizontally (x-direction) polarized source, the electric field at a point $R(x, y, z)$ in the far field can be obtained by summing the scalar electric fields of the rays from all the images as

$$E_r^H(x, y, z) = \sum_{u=-\infty}^{+\infty} \sum_{v=-\infty}^{+\infty} \frac{e^{-jkr_{u,v}}}{r_{u,v}} \rho_{//}^{|u|} \rho_{\perp}^{|v|} \tag{31}$$

where

$$r_{u,v} = \sqrt{(x_u - x)^2 + (y_v - y)^2 + z^2} \tag{32}$$

represents the distance between the observation point R and the image $\mathrm{I}_{u,v}$. $\rho_{\perp,//}$ are the reflection coefficients defined in (19). The

incidence angle $\theta_{\perp,//}$ and surface impedance factor $\Delta_{\perp,//}$ in (19) for a horizontally polarized source can be readily calculated as

$$\begin{aligned} \theta_{\perp} &= \operatorname{acos}\left(|y_v - y|/r_{u,v}\right) \\ \theta_{//} &= \operatorname{acos}\left(|x_u - x|/r_{u,v}\right) \end{aligned} \tag{33}$$

$$\begin{aligned} \Delta_{\perp} &= \sqrt{\bar{\varepsilon}_b - \sin^2\theta_{\perp}} \\ \Delta_{//} &= \frac{\sqrt{\bar{\varepsilon}_a - \sin^2\theta_{//}}}{\bar{\varepsilon}_a} \end{aligned} \tag{34}$$

3.2.2. Vertical Polarization

Following a similar procedure, the electrical field at $R(x, y, z)$ for a vertically polarized source can be expressed as

$$E_r^V(x, y, z) = \sum_{u=-\infty}^{+\infty} \sum_{v=-\infty}^{+\infty} \frac{e^{-jkr_{u,v}}}{r_{u,v}} \rho_{\perp}^{|u|} \rho_{//}^{|v|} \tag{35}$$

Eq. (35) appears to be similar to (31); however, special care must be taken to compute the reflection coefficients $\rho_{\perp,//}$ in (35). The same equation of (19) can be used to compute the reflection coefficients $\rho_{\perp,//}$ in (35), but the corresponding variables in (35), $\theta_{\perp,//}$ and $\Delta_{\perp,//}$, become

$$\begin{aligned} \theta_{//} &= \operatorname{acos}\left(|y_v - y|/r_{u,v}\right) \\ \theta_{\perp} &= \operatorname{acos}\left(|x_u - x|/r_{u,v}\right) \end{aligned} \tag{36}$$

$$\begin{aligned} \Delta_{//} &= \frac{\sqrt{\bar{\varepsilon}_b - \sin^2\theta_{//}}}{\bar{\varepsilon}_b} \\ \Delta_{\perp} &= \sqrt{\bar{\varepsilon}_a - \sin^2\theta_{\perp}} \end{aligned} \tag{37}$$

A close inspection of (35) and (31) shows that the electrical field expressions corresponding to the vertical and horizontal polarizations can be converted from one to the other by switching "x" to "y", "u" to "v", and "$\bar{\varepsilon}_a$" to "$\bar{\varepsilon}_b$", or vice versa. This can be explained by the relative rotation principle: Usually switching the polarization from one to the other is implemented by rotating the antenna in the tunnel, which is equivalent to rotating the tunnel and coordinate system while keeping the antenna unchanged.

3.2.3. Ray Tracing Discussion

It is worthwhile to note that the geometric ray in Section 3 is different from the ray presented in Section 2. The geometric rays in this section are launched from a specific point source, either from the source or its images, and are mathematically represented by a spherical wave. In contrast, the rays in Section 2 are mathematically represented by a plane wave, without any specific sources.

By considering the vector nature of the electric field, (31) and (35) cannot give an accurate electrical field prediction when the receiver is in the vicinity of the transmitter. When near the transmitter, the vector sum of electric field components should be used instead of the scalar summation shown in (31). Another important factor that has been neglected in (31) under the far zone assumption, but has to be taken into account when the receiver is near the transmitter, is the antenna pattern function, as will be shown in the following analysis.

4. CONSIDERATION ANTENNA EFFECTS

In our previous discussion, the electric fields have been normalized. In a practical communication system, the transmitted power usually is known. The electric field corresponding to a fixed transmitted power of P_t can be represented by

$$E_{u,v}^{V} = \sqrt{\frac{\eta P_t}{2\pi}} f_t\left(\theta_{u,v}, \phi_{u,v}\right) \frac{e^{-jkr_{u,v}}}{r_{u,v}} \rho_{\perp}^{|u|} \rho_{//}^{|v|} \tag{38}$$

where $f_t(\theta_{u,v}, \phi_{u,v})$ is the pattern function of the transmitting antenna. $\theta_{u,v}$ and $\phi_{u,v}$ (in spherical coordinates) are the radiating angles of the ray that is virtually from the image $I_{m,n}$, and η is the wave impedance of the free space. The effective antenna area for the receiving antenna can be expressed as

$$A_e = \left(\frac{\lambda^2}{4\pi}\right) f_r\left(\widehat{\theta}_{u,v}, \widehat{\phi}_{u,v}\right) \tag{39}$$

where $f_r\left(\widehat{\theta}_{u,v}, \widehat{\phi}_{u,v}\right)$ is the pattern function of the receiving antenna, and the two receiving angles $\widehat{\theta}_{u,v}$ and $\widehat{\phi}_{u,v}$, may or may not equate to the radiating angles of the same ray, depending on the orientation of the transmitting and receiving antennas.

The received power can then be obtained as

$$P_r = A_e \frac{|E|^2}{2\eta} = P_t \left(\frac{\lambda}{4\pi}\right)^2 \left(\sum_{u=-\infty}^{+\infty}\sum_{v=-\infty}^{+\infty} \frac{e^{-jkr_{u,v}}}{r_{u,v}} \rho_{\perp}^{|u|} \rho_{//}^{|v|} f_r\left(\widehat{\theta}_{m,n}, \widehat{\phi}_{m,n}\right) f_t\left(\theta_{m,n}, \phi_{m,n}\right)\right)^2 \quad (40)$$

Again we assume that the receiver is sufficiently far from the transmitter so that the variation of the radiating and receiving angles are small such that the antenna gains for different rays can be approximated by a constant. In other words, the following approximation can be made:

$$\begin{aligned} f_t\left(\theta_{m,n}, \phi_{m,n}\right) &\approx \sqrt{g_t} \\ f_r\left(\widehat{\theta}_{m,n}, \widehat{\phi}_{m,n}\right) &\approx \sqrt{g_r} \end{aligned} \quad (41)$$

where $g_{t,r}$ is the antenna gain for the transmitting and receiving antennas, respectively. Under this assumption, the received power $P_r^{\perp,//}$ can be simplified as:

$$\begin{pmatrix} P_r^V \\ P_r^H \end{pmatrix} = P_t g_t g_r \left(\frac{\lambda}{4\pi}\right)^2 \begin{pmatrix} E_r^V \\ E_r^H \end{pmatrix}^2 \quad (42)$$

After the power distribution along the tunnel is obtained, the attenuation constant of the dominant mode can be calculated based on fitting algorithms such as the linear least squares fitting.

It should be noted that the same antenna effect should also be considered in the modal method as discussed in Section 1, since antennas are usually involved in the radiating of RF signals. With the antenna effect, the power for the dominant mode in the far field becomes:

$$\begin{pmatrix} P_{1,1}^V \\ P_{1.1}^H \end{pmatrix} = P_t g_t g_r \left(\frac{\lambda}{4\pi}\right)^2 \begin{pmatrix} e^{-2z\alpha_{1,1}^V} \\ e^{-2z\alpha_{1,1}^H} \end{pmatrix} \quad (43)$$

Substituting (26) and (28) into (42), the power attenuation constant with the antenna effect included can be expressed as

$$\begin{pmatrix} \hat{\alpha}_{1,1}^V \\ \hat{\alpha}_{1,1}^H \end{pmatrix} = -10\log_{10}\left[\begin{array}{c} P_{1,1}^V(z)/\left(zP_{1,1}^V(0)\right) \\ P_{1,1}^H(z)/\left(zP_{1,1}^H(0)\right) \end{array}\right] = -8.686 \begin{pmatrix} \alpha_{1,1}^V \\ \alpha_{1,1}^H \end{pmatrix} \quad (44)$$

Note that the power attenuation constants in (44) are exactly the same as their expressions in (27) or (29) in which the antenna effect is not included. This suggests that the frequency dependency caused by antenna effect is only needed when calculating the absolute receiving power but does not affect the calculation of the power attenuation constant.

5. SOME NUMERICAL RESULTS AND DISCUSSION

The closed form expression of the attenuation constant in (26) or (28), although approximated, provides good insight into the analysis of the power loss in a practical dielectric tunnel. It is shown that the attenuation constant of a radio wave is mainly determined by the following parameters: the polarization and frequency of the signal, complex permittivity $\bar{\varepsilon}_{a,b}$, and dimensions of the tunnel. We will investigate each of these parameters, with the goal of investigating what can be learned from their optimum values for the minimum power attenuation.

5.1. Impact of Polarization

Assuming $\bar{\varepsilon}_a = \bar{\varepsilon}_b = \bar{\varepsilon}$ and subtracting (28) from (26), the difference of the attenuation constants corresponding to the vertical and horizontal polarizations can be written as:

$$\Delta\alpha_{1,1} = \alpha_{1,1}^H - \alpha_{1,1}^V = \frac{\lambda^2 \mathrm{Re}\left\{\sqrt{\bar{\varepsilon}-1}\right\}}{16}\left(\frac{1}{a^3} - \frac{1}{b^3}\right) \tag{45}$$

It is apparent that in narrow and high tunnels where $a < b$, vertically polarized signals attenuate less as compared to horizontally polarized signals. The opposite is true for wide and low tunnels where $a > b$.

Generally, to achieve the minimum loss in a rectangular tunnel, the direction of the E field should coincide with the larger transverse dimension of the tunnel.

5.2. Impact of Frequency

Based on (27), it is clear that the power loss (in dB/m) in a straight tunnel is inversely proportional to the square of the frequency. Theoretically, the attenuation can be made arbitrarily small by choosing a sufficiently high frequency. In other words, there is no "optimum frequency" for the minimum loss in a dielectric waveguide. Instead, to achieve the minimum loss, the highest frequency allowable should be used. It should be noted that this statement is true only for an ideal waveguide with uniform cross section along the whole tunnel. In reality, the existence of other factors such as long range tilt of the tunnel [10] may introduce additional power attenuation that is proportional to the frequency. As a result, optimum frequencies may exist as a balance of different conflicting factors. Such optimum frequencies, if they exist, would be highly dependent on the geometry of the tunnel, and thus likely vary for different tunnels.

Additionally, a small angle approximation associated with grazing incidence has been made during the derivation of (26). It is known that the grazing incidence assumption is only valid when the wavelength is small as compared to the tunnel dimensions. To calculate the error caused by approximations made in the derivation of (26), the true value of the attenuation constant with little or no approximations is required. It is shown in [10, 19, 31] that the "exact solution" of the attenuation constant can be obtained by numerically solving the equations imposed by the boundary conditions. Specifically, the complex wave vector component $\tilde{k}_{x,y}$ in (3) can be calculated by numerically solving the following complex equations:

$$\begin{aligned} \tilde{k}_x \tan \tilde{k}_x a &= jk\sqrt{\frac{(\bar{\varepsilon}_a - 1)}{\bar{\varepsilon}_a^2}} \\ \tilde{k}_y \tan \tilde{k}_y b &= jk\sqrt{(\bar{\varepsilon}_b - 1)} \end{aligned} \tag{46}$$

for a horizontal (x) polarized signal and

$$\begin{aligned} \tilde{k}_x \tan \tilde{k}_x a &= jk\sqrt{(\bar{\varepsilon}_a - 1)} \\ \tilde{k}_y \tan \tilde{k}_y b &= jk\sqrt{\frac{(\bar{\varepsilon}_b - 1)}{\bar{\varepsilon}_b^2}} \end{aligned} \tag{47}$$

for a vertical (y) polarized signal. The attenuation constant then can be obtained by taking the imagery part of the $\tilde{k}_z$ as:

$$\alpha_{m,n} = -\mathrm{Im}\left\{\sqrt{k^2 - \tilde{k}_x^2 - \tilde{k}_y^2}\right\} \tag{48}$$

Figure 3 shows how the exact and approximated attenuation constants vary with the frequency. The exact result is obtained by solving the boundary equations in (46) and (47) with Matlab using Newton's method, and the approximated result is computed directly based on the analytical form in (26) and (28). It is shown that the approximation error increases as the frequency decreases. The large approximation error in the low frequency regime implies that the analytical form is not accurate for estimating the propagation loss when the frequency is low.

In this specific example where the width of tunnel is larger than the height, the approximation error of a vertically polarized signal is larger than that of a horizontally polarized signal. In general, the approximation error is worse when the electric field is aligned with the short dimension of the tunnel. Additionally, the approximation error significantly increases for higher order modes as compared to the dominant mode.

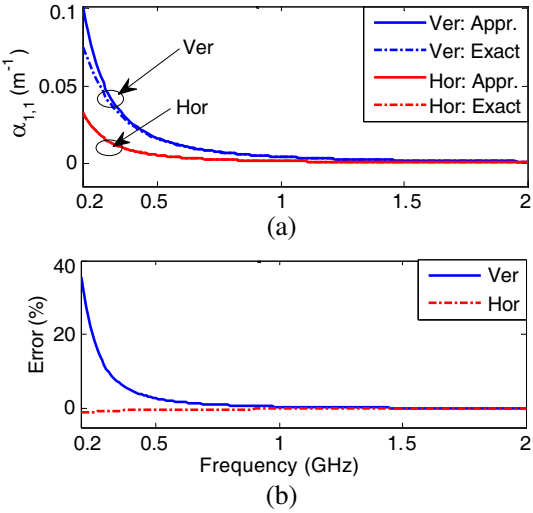

Figure 3. The attenuation constants of the dominant mode for vertically and horizontally polarized signals decrease as the frequency increases. (a) shows a comparison between the approximated solution (calculated based on the closed form expression given in (26) and (28)) and the exact solution (obtained by numerically solving (46) and (47)). (b) gives the difference between the approximated value and the exact value, expressed in a percentage of the exact value.

Table 1. parameters used in the numerical results.

a	10 feet	$\bar{\varepsilon}_a$	5
b	5 feet	$\bar{\varepsilon}_b$	5
σ_a	0	σ_a	0

5.3. Optimum Dimension Ratio

Equation (27) dictates that the tunnel cross-sectional dimensions are the two most important parameters since the attenuation constant varies inversely with the cube of the dimensions, as compared to square of the frequency and approximately square root of the permittivity. A small change in tunnel dimensions leads to a significant change in the attenuation constant. Likewise, given a fixed system frequency and tunnel wall material, tunnels with big cross-sectional area generally lead to smaller attenuation constants. On the other hand, for a fixed

cross-sectional area, the attenuation constant varies with the exact shape of the cross section. One interesting question would be how the attenuation constant varies with the ratio of the dimensions, given a fixed rectangular area of the cross section. Specifically, one may be interested to know if there is an optimum dimension ratio for the minimum power loss.

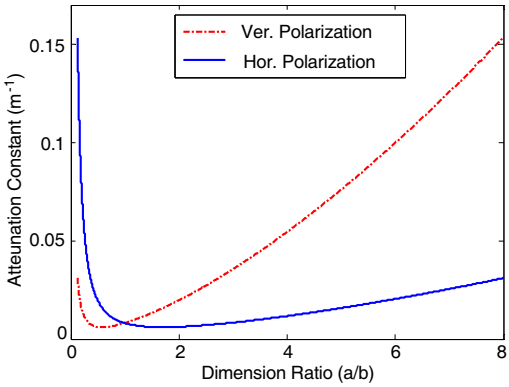

Figure 4. Attenuation constant of the dominant mode ($EH_{1,1}$) varies with the ratio of the transverse dimensions for a fixed rectangular cross-sectional area.

Figure 4 shows how the attenuation constant of the dominant $EH_{1,1}$ mode changes with the ratio of the dimensions, while the area of the rectangular cross section is kept constant at $200\,\mathrm{ft}^2$ ($18.58\,\mathrm{m}^2$). The frequency selected is 915 MHz. The other parameters used in the simulation are given in Table 1. It is evident from Fig. 4 that under the same area assumption, both "ultra-wide" and "ultra-narrow" tunnels cause high propagation loss and thus may not be suited for radio communications at these frequencies.

It is found that an optimum dimension ratio exists for both vertically and horizontally polarized signals. An inspection of the optimized values shows that the minimum attention constants ($0.0061\,\mathrm{m}^{-1}$) for the two polarizations cases are the same while the dimension ratios for achieving the minimum loss are reciprocal.

In the following, we will derive the analytical form of the optimum dimension ratio defined as

$$\zeta = \frac{d_E}{d_o} \tag{49}$$

where d_E is the dimension that the dominant E field coincides with and d_o is the other transverse dimension of the tunnel. Specifically, we

have

$$\zeta = \begin{cases} b/a, & \text{for vertical polarization} \\ a/b, & \text{for horizontal polarization} \end{cases} \tag{50}$$

For a given cross-sectional area S, (26) becomes

$$\begin{aligned} \alpha_{m,n}^{H} &= \frac{S^{-\frac{3}{2}}\zeta^{-\frac{3}{2}}(m\lambda)^2}{2}\mathrm{Re}\left\{\frac{\bar{\varepsilon}_a}{\sqrt{\bar{\varepsilon}_a-1}}\right\} \\ &\quad + \frac{S^{-\frac{3}{2}}\zeta^{\frac{3}{2}}(n\lambda)^2}{2}\mathrm{Re}\left\{\frac{1}{\sqrt{\bar{\varepsilon}_b-1}}\right\} \end{aligned} \tag{51}$$

By setting the partial derivative of the attenuation constant $\alpha_{m,n}^{H}$ relative to ζ as zero, the optimum dimension ratio can be obtained as

$$\zeta_{opt}^{H} = \sqrt[3]{\left(\frac{m}{n}\right)^2 \mathrm{Re}\left\{\frac{\bar{\varepsilon}_a\sqrt{\bar{\varepsilon}_b-1}}{\sqrt{\bar{\varepsilon}_a-1}}\right\}} \tag{52}$$

Considering a special case of $\bar{\varepsilon}_b = \bar{\varepsilon}_a = \bar{\varepsilon}$, the optimum dimension ratio for the dominant $EH_{1,1}$ mode can be simplified as

$$\zeta_{opt}^{H} = \mathrm{Re}\left\{\bar{\varepsilon}^{\frac{1}{3}}\right\} \tag{53}$$

It is found that, although a special case of rectangles, a square tunnel is unlikely to be the optimum tunnel since the relative dielectric constant in (53) is always larger than one.

Similarly, for the vertical polarization case, we have

$$\zeta_{opt}^{V} = \mathrm{Re}\left\{\bar{\varepsilon}^{\frac{1}{3}}\right\} \tag{54}$$

which has the exactly same form as the horizontal polarization case. As a cross check, substituting $\bar{\varepsilon} = 5$ into (53) and (54) leads to the same optimum ratio ($\zeta_{opt}^{H} = 0.585$) for both the horizontal and vertical polarizations. Considering the different definitions of ζ for the two polarizations, the results computed with the analytical forms are consistent with the numerical results shown in Fig. 4.

It should be noted that most of the materials in our daily life have a relative permittivity ranging from 2 to 20 which corresponds to an optimum dimension ratio of ζ_{opt}^{V} spanning from 1.4 to 2.7.

In summary, to achieve the minimum attenuation, the ratio of the larger transverse dimension to the smaller transverse dimension should be designed as $\sqrt[3]{\bar{\varepsilon}}$, and the dominant electric field should always coincide with the larger dimension. This optimum dimension ratio holds independent of the frequency, as long as the tunnel dimensions are much larger than the wavelength of interest such that the attenuation constants in (26) and (28) give accurate prediction of propagation loss.

5.4. Optimum Dielectric Constant for Given Dimensions

The impact of the tunnel permittivity on the attenuation constant is relatively small compared to the frequency and tunnel dimensions. With the same parameters described in Table 1, Fig. 5 shows how the attenuation constant of the dominant mode varies with the relative dielectric constant. Given fixed tunnel dimensions, it is shown that an "optimum" relative dielectric constant exists for both polarizations. It is also found that the attenuation constant of the horizontal polarized signals is relatively insensitive to the variation the dielectric constant when the dielectric constant is sufficiently large (larger than 5 in this specific example). Again, by assuming $\bar{\varepsilon}_b = \bar{\varepsilon}_a = \bar{\varepsilon}$, the optimum relative dielectric constant $\bar{\varepsilon}_{opt}$ for the dominant mode can be readily obtained by calculating the stationary point of (26) and (28) relative to $\bar{\varepsilon}$ as

$$\bar{\varepsilon}_{opt} = 2 + \zeta^3 \tag{55}$$

It is observed from (55) that the minimum $\bar{\varepsilon}_{opt}$ can be a very large number, depending on the ratio of the tunnel dimensions, but has an minimum value of 2. As a cross check, substituting $a = 10\,\text{ft}$ and $b = 5\,\text{ft}$ into the analytical form in (55) gives $\bar{\varepsilon}_{opt} = 10$ for horizontally polarized signals and $\bar{\varepsilon}_{opt} = 2.1$ for vertically polarized signals. Those optimum values are consistent with the numerical results shown in Fig. 5.

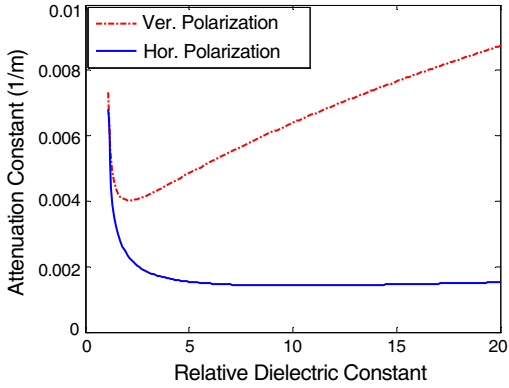

Figure 5. Attenuation constant of the dominant mode ($EH_{1,1}$) varies with the dielectric constant.

5.5. Impact of Conductivity

The impact of the conductivity can be treated as part of the permittivity impact since the conductivity contributes to the imaginary part of the complex dielectric constant as:

$$\bar{\varepsilon}_{a,b} = \varepsilon_{a,b} - j\frac{\sigma_{a,b}}{2\pi f \varepsilon_0} \tag{56}$$

If the frequencies of interest are sufficiently high, the imaginary part of $\bar{\varepsilon}_{a,b}$ approaches zero. Therefore, the impact of the conductivity is often ignored in the high frequency regime. In the following we will investigate the impact of the conductivity on the attenuation constant when the frequency is relatively low. Again, we will first consider the horizontal polarization case and the results obtained can be readily generalized to the vertical polarization case by exchanging "m" with "n" and "a" with "b" in the final analytical form obtained. For the low frequency regime shown in Fig. 3, the classic form of the attenuation constant given in (26) is not an accurate representation of the true value due to high approximation errors. A more accurate form will be sought at these frequencies. An inspection of boundary equation (46) shows that an approximated analytical solution can be obtained by making the following approximations [19]:

$$\begin{aligned} \tilde{k}_x a &\approx \frac{m\pi}{2} + \delta_x \\ \tilde{k}_y b &\approx \frac{n\pi}{2} + \delta_y \end{aligned} \tag{57}$$

where $\delta_{x,y}$ are two small complex terms to be determined. Substituting (57) into (46) and solving for $\delta_{x,y}$ yields:

$$\begin{aligned} \delta_x &\approx \frac{j\bar{\varepsilon}_a}{ka\sqrt{\bar{\varepsilon}_a - 1}} k_x \\ \delta_y &\approx \frac{j}{kb\sqrt{\bar{\varepsilon}_b - 1}} k_y \end{aligned} \tag{58}$$

Substituting (58) back into (57) leads to:

$$\begin{aligned} \tilde{k}_x &\approx \frac{m\pi}{2a} + \frac{jm\lambda\bar{\varepsilon}_a}{4a^2\sqrt{\bar{\varepsilon}_a - 1}} \\ \tilde{k}_y &\approx \frac{n\pi}{2b} + \frac{jn\lambda}{4b^2\sqrt{\bar{\varepsilon}_b - 1}} \end{aligned} \tag{59}$$

Note that (59) here is identical to the results in (4) which are simplified based on the analytical expressions from [16].

Assuming that $\tilde{k}_{x,y}$ are small compared to k and substituting (59) into (48) gives:

$$\begin{aligned}
\alpha_{m,n} &= -\mathrm{Im}\left\{\sqrt{k^2-\tilde{k}_x^2-\tilde{k}_y^2}\right\} \\
&\approx -\mathrm{Im}\left\{k\left(1-\frac{\tilde{k}_x^2+\tilde{k}_y^2}{2k^2}\right)\right\} \\
&= \mathrm{Im}\left\{\frac{\tilde{k}_x^2+\tilde{k}_y^2}{2k}\right\} \\
&= \frac{2\pi}{\lambda}\left[\mathrm{Re}\left\{\tilde{k}_x\right\}\mathrm{Im}\left\{\tilde{k}_x\right\}+\mathrm{Re}\left\{\tilde{k}_y\right\}\mathrm{Im}\left\{\tilde{k}_y\right\}\right] \qquad (60)
\end{aligned}$$

Substituting (59) into (60) and after some mathematical manipulations, we have:

$$\begin{aligned}
\alpha_{m,n}^{H} &= \frac{1}{a}\left(\frac{m\lambda}{4a}\right)^2 \mathrm{Re}\left\{\frac{\bar{\varepsilon}_a}{\sqrt{\bar{\varepsilon}_a-1}}\right\}[1-\delta_a] \\
&\quad +\frac{1}{b}\left(\frac{n\lambda}{4b}\right)^2 \mathrm{Re}\left\{\frac{1}{\sqrt{\bar{\varepsilon}_b-1}}\right\}[1-\delta_b] \qquad (61)
\end{aligned}$$

where

$$\begin{aligned}
\delta_a &= \frac{1}{ka}\mathrm{Im}\left\{\frac{\bar{\varepsilon}_a}{\sqrt{\bar{\varepsilon}_a-1}}\right\} \\
\delta_b &= \frac{1}{kb}\mathrm{Im}\left\{\frac{1}{\sqrt{\bar{\varepsilon}_b-1}}\right\} \qquad (62)
\end{aligned}$$

A comparison of (61) with its classic but approximated form in (27) shows that the two forms are identical except for the two small correction terms $\delta_{a,b}$ in (61) which are introduced to compensate for the impact of the conductivity. As a special case where the conductivity of the tunnel walls is zero, (61) reduces to its classic form in (27). Additionally, it is shown in (61) and (62) that the contribution of $\delta_{a,b}$ can be neglected if the tunnel transverse dimensions are electrically large such that $ka \gg 1$ and $kb \gg 1$.

Figure 6 illustrates the impact of the conductivity on the attenuation constant of the dominant mode. The Y axis in Fig. 6 represents the error in the attenuation constant caused by neglecting the conductivity of the wall materials. The error is given as a percentage of the true attenuation constant which is calculated by including the conductivity. Again, the parameters in Table 1 are used for calculating the values of errors in Fig. 6. It is shown that the impact of the conductivity increases with the value of the conductivity

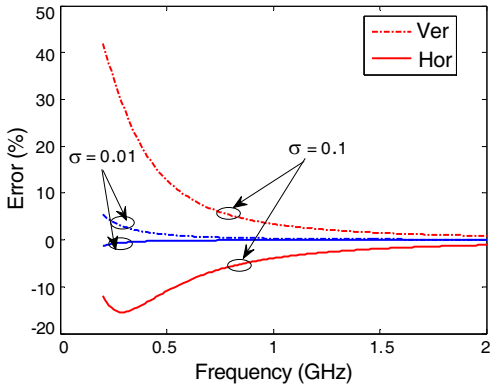

Figure 6. Impact of conductivity on the attenuation constant.

but decreases as the frequency increases. For frequencies above 1 GHz, the error caused by ignoring the conductivity is less than 5%, even when the conductivity is as high as 0.1 S/m. This observation suggests that the impact of conductivity can be neglected when the frequency of interest is above 1 GHz.

6. ATTENUATION CONSTANT MEASUREMENT

RF power measurements were made along a straight concrete tunnel with its geometric dimensions shown in Fig. 7. The four walls of the tunnel are relatively smooth so the impact of wall roughness on the attenuation constant can be neglected. Measurements were made at four different frequencies (455, 915, 2450, 5800 MHz) for both vertical and horizontal polarizations. Except for the first frequency of 455 MHz which is often used in underground UHF leaky feeder systems, the other three test frequencies are commonly used in commercially available underground coal mine communication systems. The length of tunnel is about 610 m.

A block diagram of the measurement setup is shown in Fig. 8(a), and a picture of the equipment in Fig. 8(b). It is comprised of two components: a stationary RF transmitter and a mobile RF receiver. The transmitter consists of an RF signal source connected to one of four linear polarized antennas (Laird FG4500, FG8960, FG24005, and SuperPass SPDJ40) or an Agilent V3500A RF power meter. The antennas at the transmitter and receiver were set to the same height of 1.2 m and were located in the center between the two side walls during measurements.

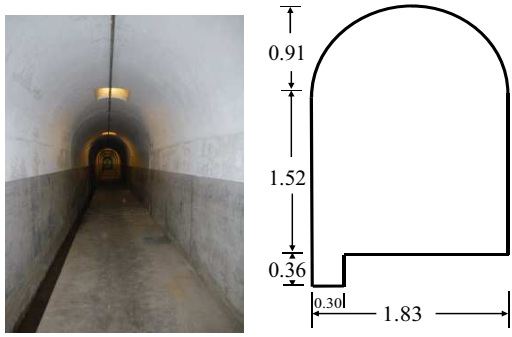

Figure 7. A picture of the measured tunnel (left) and the geometric dimensions of the tunnel in units of meters.

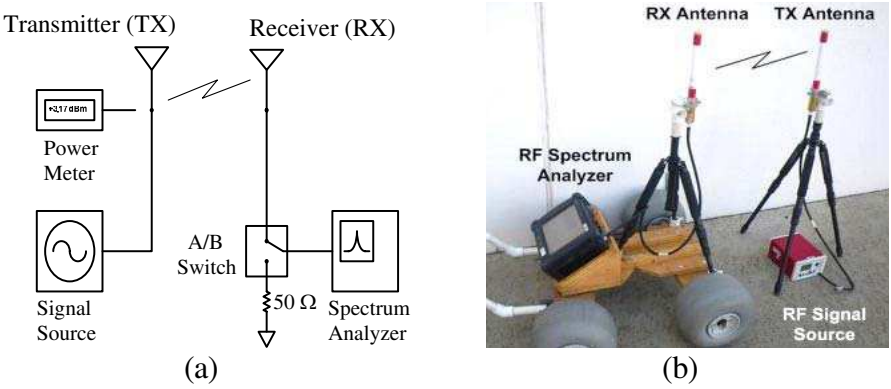

Figure 8. Experimental setup.

The receiver consists of a Tektronix H600 data-logging RF spectrum analyzer connected to either a 50 Ω termination or matching TX antenna through an RF A/B switch. The receiver is mounted on a small wooden cart with plastic wheels shown in Fig. 8(b).

RF signal propagation was measured as follows: The RF signal source was configured to produce a continuous wave (CW) signal with a fixed output power (about 3 dBm) which was verified at the beginning of each propagation measurement using the RF power meter. The spectrum analyzer's input was switched to the RX antenna and the mobile receiver cart was pulled away from the transmitter. At pre-surveyed intervals of distance — typically 30 m — the mobile receiver cart was halted and the spectrum analyzer's input was momentarily switched to the 50 Ω termination. This inserted a received power null

in the measured data, serving as a distance indicator. The spectrum analyzer's input was then switched back to the RX antenna and travel away from the transmitter was resumed. Post-processing of the logged data was performed to correlate the power nulls in the data to the pre-surveyed distances [14].

7. COMPARING SIMULATION TO MEASUREMENT

Figures 9 and 10 show a comparison between the measured and simulated power decay along the tunnel axial distance for the vertical and horizontal polarization cases, respectively. The blue solid line represents the measured results and the red dotted line the simulated results which are calculated based on (42), the ray tracing model described in Section 3. It is generally observed [17, 32, 33] that propagation can be divided into two regions: the near zone and far zone. The signal power fluctuates widely with the distance in the near zone [34] while it is relatively stable and thus more predictable in the far zone. After a certain distance that is sufficiently far from

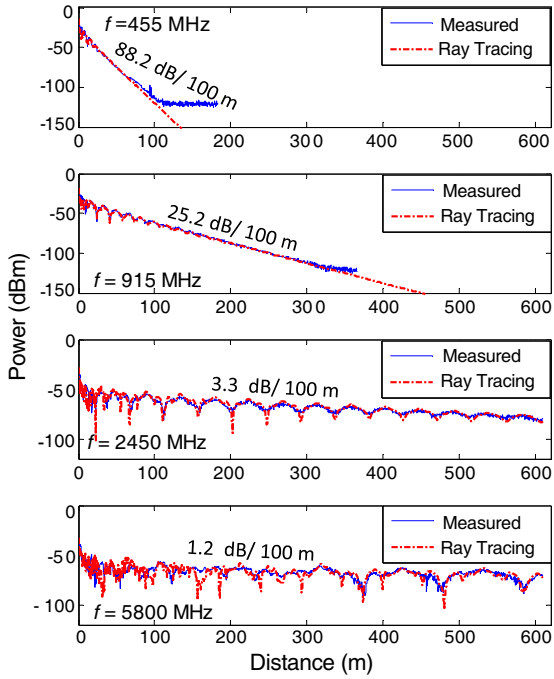

Figure 9. A comparison between measured and simulated power decay along the tunnel at four test frequencies (horizontal polarization).

the transmitter, the power (in a dB scale) decays linearly with the distance. The point separating the near zone and far zone is the breaking point [35], which moves closer to the transmitter as the frequency decreases. As a result, a very small near zone distance is observed at 455 MHz. It should be noted that the linear attenuation behavior is an indication of the single mode (the lowest attenuated mode) dominance. Some pseudo-periodic behaviors can be found before the linear attenuation region. From the modal theory, those quasi-periodic behaviors are known to be caused by the interaction of a few lowest modes. Additionally, because the power attenuates so quickly at 455 MHz, it reaches the noise power level (about −120 dBm) of the equipment after a short distance, causing it remain flat over the distance, as shown in Fig. 9 and Fig. 10.

In the modeling results shown, the arched tunnel shown in Fig. 7 was approximated by a rectangular tunnel with the same width. The height, along with the electrical parameters of the tunnel, was optimized based on minimizing the difference between the theoretical and measured attenuation constant of the dominant mode. The

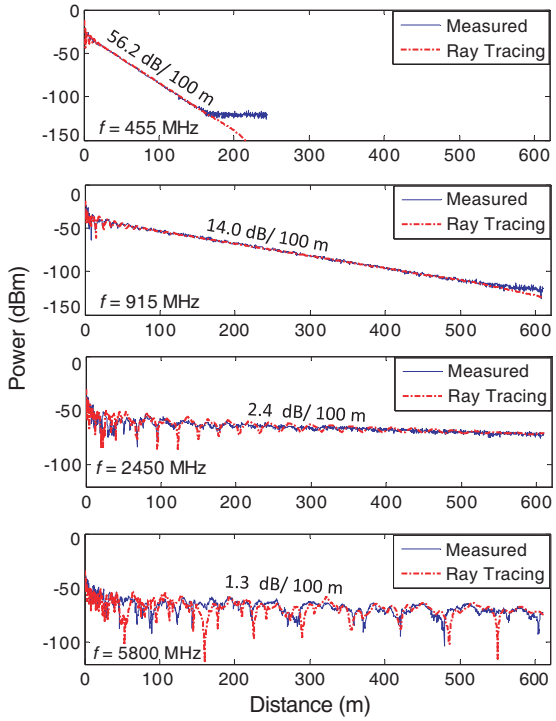

Figure 10. A comparison between measured and simulated power decay along the tunnel at four test frequencies (vertical polarization).

simulated power at the zero distance was adjusted to best match the measured power distribution. The measured attenuation constant of the dominant mode was estimated by applying linear least squares fitting to the measured power decay at large distances (far zone). It should be noted that, due to the limitation of the tunnel length, this estimation is likely not accurate at the frequency of 5.8 GHz, because the linear attenuation of the power decay does not appear even at the end of the tunnel. The following data set is found to be the best match of the theoretical results to the measured results: $\bar{\varepsilon} = 8.9$ and $\sigma = 0.15\,\mathrm{S/m}$, $h = 2.35\,\mathrm{m}$. This same data set has been used for predicting the power decay for both the vertical and horizontal polarization cases. Additionally, the absolute values of both m and n in (31) and (35) have been limited to 40 since rays undergoing a large number of reflections within the interested distance range in this paper essentially make little contribution to the overall power and thus can be ignored. It is shown in both figures that the ray model results match the measured results well in the far zone, at all the four tested frequencies, and for both polarizations. The good agreement between the measured and simulated curves suggests that the ray tracing model is a good model for predicting the power attenuation in this tunnel environment.

A comparison of the attenuation constant at different frequencies and polarizations is shown in Fig. 11. The ray tracing based attenuation constant is extracted from the simulated power decay by employing the same linear fitting as used for estimating the attenuation constant of the measurement results. In contrast to the measured power decay which is limited by the physical length of the tunnel, the

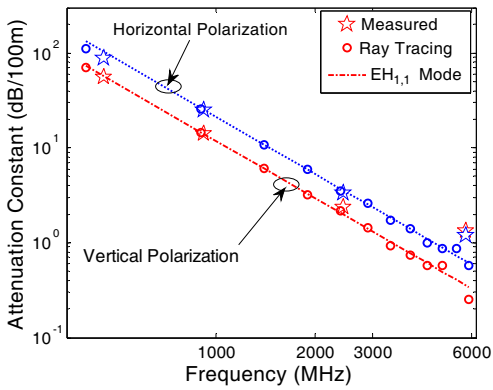

Figure 11. A comparison between the measured and simulated attenuation constants at different frequencies. Note that both of the axes are shown in a logarithmic scale with respect to the base of 10.

simulated power decay can be extended to a sufficiently long distance such that the linear attenuation with the distance appears. The two dash lines in Fig. 11 are calculated based on (44) which provides the analytical form of the attenuation constant for the dominant EH_{11} mode. The same electrical parameters are used for both the simulated (ray tracing based) and analytical results. It is shown that the simulated, measured, and analytical results agree well with each other. Note a small discrepancy appears between the measured and simulated attenuation values at 5.8 GHz. This is due to the fact that significant nulls exist along the tunnel at these high frequencies, which increases the uncertainty in the determination of the best linear fitting to the measured data.

8. CONCLUSION

When a ray is incident on a dielectric tunnel wall, part of the energy "leaks" into the wall and part is reflected back to the tunnel. Therefore the energy loss associated with the RF propagation in a dielectric tunnel should be highly dependent on the reflection coefficient of the ray. In this paper, we have mathematically established this connection between the power attenuation constant and the classic Fresnel reflection coefficient, by showing that the attenuation constants of different modes in an empty dielectric tunnel can be derived based on the reflection coefficients associated with the characteristic rays of the corresponding mode. The new derivation provides good insight into understanding the controlling factors of the RF attenuation in tunnels which have been discussed in detail. Measurements at different frequencies that are commonly used in commercially available underground coal mine communication systems validated the model. The simulated power distributions match the measured ones at all four tested frequencies and for both horizontal and vertical polarizations. Furthermore, we compared the attenuation constants calculated from the ray tracing and modal methods and showed they agree well with each other. The simulated attenuation constants based on the two methods are also shown to be consistent with the measured ones.

DISCLAIMER

The findings and conclusions in this paper are those of the authors and do not necessarily represent the views of the National Institute for Occupational Safety and Health (NIOSH). Mention of any company name or product does not constitute endorsement by NIOSH.

REFERENCES

1. Mazar, R., A. Bronshtein, and I. T. Lu, "Theoretical analysis of UHF propagation in a city street modeled as a random multislit waveguide," *IEEE Transactions on Antennas and Propagation*, Vol. 46, 864–871, Jun. 1998.
2. Porrat, D., "Radio propagation in hallways and streets for UHF communications," Ph.D. Dissertation, Stanford University, 2002.
3. Kyritsi, P. and D. C. Cox, "Propagation characteristics of horizontally and vertically polarized electric fields in an indoor environment: Simple model and results," *IEEE 54th Vehicular Technology Conference, VTC Fall*, 1422–1426, 2001.
4. Didascalou, D., R. Maurer, and W. Wiesbeck, "Subway tunnel guided electromagnetic wave propagation at mobile communications frequencies," *IEEE Transactions on Antennas and Propagation,* Vol. 49, 1590–1596, Nov. 2001.
5. Masson, E., Y. Cocheril, P. Combeau, L. Aveneau, M. Berbineau, R. Vauzelle, et al., "Radio wave propagation in curved rectangular tunnels at 5.8 GHz for metro applications, simulations and measurements," *Eurasip Journal on Wireless Communications and Networking*, Dec. 2011.
6. Zhang, Y. P., Z. R. Jiang, T. S. Ng, and J. H. Sheng, "Measurements of the propagation of UHF radio waves on an underground railway train," *IEEE Transactions on Vehicular Technology*, Vol. 49, 1342–1347, Jul. 2000.
7. Han, G. R., W. M. Zhang, and Y. P. Zhang, "An experiment study of the propagation of radio waves in a scaled model of long-wall coal mining tunnels," *IEEE Antennas and Wireless Propagation Letters*, Vol. 8, 502–504, 2009.
8. Lienard, M. and P. Degauque, "Natural wave propagation in mine environments," *IEEE Transactions on Antennas and Propagation*, Vol. 48, 1326–1339, Sep. 2000.
9. Shanklin, J. P., "VHF railroad communications in tunnels," *Communications,* Vol. 27, 16–19, Jun. 1947.
10. Emslie, A., R. Lagace, and P. Strong, "Theory of the propagation of UHF radio waves in coal mine tunnels," *IEEE Transactions on Antennas and Propagation*, Vol. 23, 192–205, 1975.
11. Mahmoud, S. F. and J. R. Wait, "Geometrical optical approach for electromagnetic wave propagation in rectangular mine tunnels," *Radio Science,* Vol. 9, 1147–1158, 1974.
12. United States Public Laws, PL 109-236, *Mine Improvement and New Emergency Response Act of 2006 (MINER Act)*, 2006.

13. Zhou, C., J. Waynert, T. Plass, and R. Jacksha, "Modeling RF propagation in tunnels," *IEEE International Symposium on Antennas and Propagation (APS2013)*, 1917–1918, Orlando, FL, 2013.
14. Plass, T., R. Jacksha, J. Waynert, and C. Zhou, "Measurement of RF propagation in tunnels," *IEEE International Symposium on Antennas and Propagation (APS 2013)*, 1604–1605, Orlando, FL, 2013.
15. Marcatili, E. A. J. and R. A. Schemeltzer, "Hollow metallic and dielectric waveguides for long distance optical transmission and lasers," *Bell Syst. Tech. J.,* Vol. 43, 1783–1809, Jul. 1964.
16. Laakmann, K. D. and W. H. Steier, "Waveguides: Characteristic models of hollow rectangular dielectric waveguides," *Applied Optics,* Vol. 15, 1334–1340, May 1976.
17. Dudley, D. G., M. Lienard, S. F. Mahmoud, and P. Degauque, "Wireless propagation in tunnels," *IEEE Antennas and Propagation Magazine*, Vol. 49, 11–26, Apr. 2007.
18. Didascalou, D., T. M. Schafer, F. Weinmann, and W. Wiesbeck, "Ray-density normalization for ray-optical wave propagation modeling in arbitrarily shaped tunnels," *IEEE Transactions on Antennas and Propagation,* Vol. 48, 1316–1325, Sep. 2000.
19. Mahmoud, S. F., "Modal propagation of high frequency electromagnetic waves in straight and curved tunnels within the earth," *Journal of Electromagnetic Waves and Applications,* Vol. 19, No. 12, 1611–1627, 2005.
20. Yamaguchi, Y., T. Abe, T. Sekiguchi, and J. Chiba, "Attenuation constants of UHF radio-waves in arched tunnels," *IEEE Transactions on Microwave Theory and Techniques*, Vol. 33, 714–718, 1985.
21. Kermani, M. H. and M. Kamarei, "A ray-tracing method for predicting delay spread in tunnel environments," *IEEE International Conference on Personal Wireless Communications*, 538–542, 2000.
22. Uchida, K., C. K. Lee, T. Matsunaga, T. Imai, and T. Fujii, "A ray tracing method for evaluating field distribution in tunnels," *Electronics and Communications in Japan (Part I: Communications)*, Vol. 83, 11–18, 2000.
23. Sun, Z. and I. F. Akyildiz, "Channel modeling and analysis for wireless networks in underground mines and road tunnels," *IEEE Transactions on Communications*, Vol. 58, 1758–1768, Jun. 2010.
24. Fuschini, F. and G. Falciasecca, "A mixed rays-modes approach

to the propagation in real road and railway tunnels," *IEEE Transactions on Antennas and Propagation*, Vol. 60, 1095–1105, Feb. 2012.

25. Emslie, A., R. Lagace, and P. Strong, "Theory of the propagation of UHF radio waves in coal mine tunnels," *IEEE Transactions on Antennas and Propagation*, Vol. 23, 192–205, 1975.
26. Loyka, S., "Multiantenna capacities of waveguide and cavity channels," *IEEE Transactions on Vehicular Technology*, Vol. 54, 863–872, May 2005.
27. Collin, R. E., *Field Theory of Guided Waves*, McGraw-Hill, New York, 1960.
28. Balanis, C. A., *Advanced Engineering Electromagnetics*. Wiley, New York, 1989.
29. Schaubach, K. R., N. J. Davis, and T. S. Rappaport, "A ray tracing method for predicting path loss and delay spread in microcellular environments," *IEEE 42nd Vehicular Technology Conference*, 932–935, May 1992.
30. Chen, S. H. and S. K. Jeng, "SBR image approach for radio wave propagation in tunnels with and without traffic," *IEEE Transactions on Vehicular Technology*, Vol. 45, 570–578, Aug. 1996.
31. Mahmoud, S. F., "On modal propagation of high frequency electromagnetic waves in straight and curved tunnels," *IEEE Antennas and Propagation Society Symposium*, 2963–2966, 2004.
32. Alonso, J., B. Izquierdo, and J. Romeu, "Break point analysis and modelling in subway tunnels," *3rd European Conference on Antennas and Propagation (EuCAP 2009)*, 3254–3258, 2009.
33. Dudley, D. G. and H. Y. Pao, "System identification for wireless propagation channels in tunnels," *IEEE Transactions on Antennas and Propagation*, Vol. 53, 2400–2405, Aug. 2005.
34. Guan, K., Z. D. Zhong, B. Ai, and C. Briso-Rodriguez, "Propagation mechanism analysis before the break point inside tunnels," *IEEE Vehicular Technology Conference (VTC2011 Fall)*, 1–5, Sep. 5–8, 2011.
35. Klemenschits, T. and E. Bonek, "Radio coverage of road tunnels at 900 and 1800 MHz by discrete antennas," *Wireless Networks — Catching the Mobile Future, Proceedings*, Vols. I–Iv, 411–415, 1994.